JOURNAL OF THEORETICAL AND APPLIED MECHANICS
52, 1, pp. 199-213, Warsaw 2014

A NOVEL DYNAMICAL MODEL FOR GVT NONLINEAR SUPPORTING SYSTEM WITH STABLE-QUASI-ZERO-STIFFNESS

Zhifeng Hao, Qingjie Cao

Centre for Nonlinear Dynamics Research, School of Astronautics, Harbin Institute of Technology, Harbin, China
e-mail: q.j.cao@hit.edu.cn

In this paper, a dynamical model of a spring-mass system with a single degree of freedom is proposed, which can be designed as a nonlinear supporting system for GVT of large scale aircraft and vibration isolation owing to stable-quasi-zero-stiffness (SQZS). The SQZS structure is constructed by a positive stiffness component and a pair of inclined linear springs providing negative stiffness, which is typical for an irrational restoring force due to geometrical configuration. The unperturbed analysis demonstrates complex equilibrium bifurcations and stabilities for this peculiar system, based upon which parameter optimizations are performed for SQZS and the maximum interval of low frequency. Furthermore, the dynamics analysis of the perturbed system near the optimized parameters reveals complicated behaviour of KAM structures, period doubling, chaos crisis, coexistence of multiple solutions, intermittency chaos, chaos saddle, etc. All those presented herein provide a better understanding for the complicated dynamics of SQZS nonlinear system.

Key words: stable-quasi-zero-stiffness oscillator, optimization, bifurcation and chaos

1. Introduction

Much attention has been paid on the low frequency design for GVT (ground vibration test) of large scale aircraft (Molyneux, 1957), isolation and other applications (Lorrain, 1974; Denoyer and Johnson, 2001; Winterflood, 2001; Ibrahim, 2008; Arafat *et al.*, 2010). For GVT, a low frequency supporting system is required to provide a free-free mode, where the ratio of the support natural frequency and the fundamental frequency of the aircraft to be tested should be lower than 1:3 (Green, 1945). As we have known that the fundamental frequency of a large thin-wing aircraft can be low to 1 Hz even to 0.7 Hz, which requires the supporting frequency to be lower than 0.3 Hz (Xing *et al.*, 2005). Even the earlier efforts has been made to achieve the lower frequency supporting, the conventional isolation design cannot achieve such a required low frequency, such as an undercarriage support (with 2 Hz), linear spring support (with 1 Hz), pneumatic support (with 0.5 Hz) (Molyneux, 1957; Xing *et al.*, 2005). The first conceptual design of low frequency was proposed by Molyneux (1957) with a spring geometrical arrangement to provide a zero or very low stiffness. Blair *et al.* (2002) considered ultra low frequency isolation applied to laser interferometers for gravitational wave detection. Platus (1992) adopted the negative stiffness mechanism for isolation against sub-Hertz vibrations. Zhang *et al.* (2004) utilized an isolator comprising elastic component and Euler's column providing a frequency low to 0.5 Hz. Alabuzhev *et al.* (1989) introduced a class of vibration protection designs with quasi-zero stiffness consisting of load-bearing elastic elements with constant positive stiffness as well as devices with negative stiffness. Carrella *et al.* (2007) and Kovacic *et al.* (2008) studied the force transmissibility of a quasi-zero-stiffness isolator by using the Duffing system. Most of the investigations are focused on the static design and the experiment of a low frequency system. Until recent years, Cao *et al.* (2006) proposed a model called the SD oscillator, which consists of a lump mass and a pair of inclined linear elastic springs. Several studies have been

published recently including strange attractors, Hopf bifurcation, co-dimension bifurcations and the analytical solutions (Cao *et al.*, 2008a,b; Tian *et al.*, 2010; Lai and Xiang, 2010; Cao *et al.*, 2012). These investigations showed the intrinsic characteristic of negative stiffness of the SD oscillator due to its geometrical structure, which can be applied to the dynamic design of a low frequency system.

The motivation of this paper is to propose a dynamical model for GVT nonlinear supporting system with low frequency which comprises a vertical linear spring providing a high positive stiffness as a supporting component and a SD oscillator contributing a negative stiffness. Moreover, this paper aims at the dynamical analysis to explore the complex nonlinear phenomena of the presented system, based upon which the optimum design with a maximum interval of low frequency can be achieved.

This paper is organized as follows. In Section 2, the dynamical model is proposed and formulated mathematically. In Section 3, the unperturbed dynamics of the system is presented for the complex equilibrium bifurcations. In Section 3, parameter optimization of the model is carried out for parameters μ, λ and α, γ, respectively. In the following, Section 4, dynamical analysis and numerical simulations are carried out for the system at the optimized parameters $\mu = 1$, $\lambda = 0$ to show the complex dynamical behaviour and reveal the mechanical nature of the system. This paper is ended with our conclusions and discussions.

2. Governing equation

Consider a novel model, as shown in Fig. 1, which comprises a lump mass m linked by three linear springs: a vertical spring of stiffness K_1 and the equilibrium length of H, and a pair of inclined springs of stiffness K_2 and the equilibrium length of L. The springs are capable of tension and compression pinned to each rigid support.

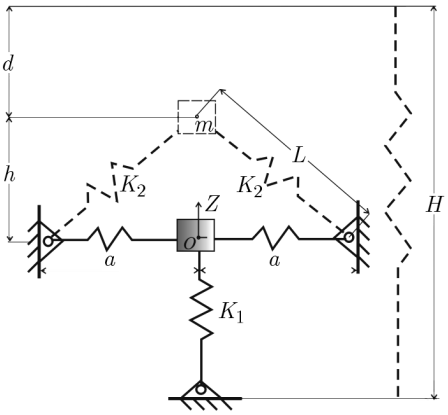

Fig. 1. Dynamical model for the mechanism of a supporting system with low frequency comprising a vertical and a pair of oblique springs

The governing equation of motion is obtained as

$$m\ddot{Z} + \Big[K_1 + 2K_2\Big(1 - \frac{L}{\sqrt{a^2 + Z^2}}\Big)\Big]Z - K_1(h + d) + mg = 0 \tag{2.1}$$

where Z is the mass displacement with respect to point O, $h + d$ the equilibrium end of the vertical spring and a the half distance between the inclined rigid supports of the springs.

The dimensionless form of system (2.1) can be obtained by letting $X = Z/L$, $\tau = \omega_0 t$, $\omega_0^2 = (K_1 + 2K_2)/m$, $\alpha = a/L$ $(\alpha \in [0, \infty))$, $\gamma = 2K_2/(K_1 + 2K_2)$ $(\gamma \in [0, 1])$ and $\eta = [K_1(h + d) - mg]/ml_1\omega_0^2$, written as

$$\ddot{X} + X - \frac{\gamma X}{\sqrt{\alpha^2 + X^2}} - \eta = 0 \tag{2.2}$$

which behaves both smooth $(\alpha > 0)$ and discontinuous $(\alpha = 0)$, in this case, system (2.2) becomes

$$\ddot{X} + X - \gamma \operatorname{sgn}(X) - \eta = 0 \tag{2.3}$$

Again, for $\alpha > 0$, system (2.1) can be rewritten in the following form by letting $x = X/\alpha$, $\mu = \gamma/\alpha$, $\lambda = \eta/\alpha$

$$\ddot{x} + x - \frac{\mu x}{\sqrt{1 + x^2}} - \lambda = 0 \tag{2.4}$$

The equivalent form of the first-order differential equations can be obtained and written as the following by letting $\dot{x} = y$,

$$\dot{x} = y \qquad \dot{y} = -x + \frac{\mu x}{\sqrt{1 + x^2}} + \lambda \tag{2.5}$$

with the potential

$$V(x) = \frac{1}{2}x^2 - \mu\sqrt{1 + x^2} - \lambda x \tag{2.6}$$

and the Hamiltonian

$$H(x, y) = \frac{1}{2}x^2 + \frac{1}{2}y^2 - \mu\sqrt{1 + x^2} - \lambda x \tag{2.7}$$

3. Unperturbed dynamics

In this Section, the unperturbed dynamics analysis of the bifurcations and stabilities of system (2.4) are presented with the equilibria, the stabilities and also the bifurcations. The equilibrium surface of system (2.4) can be obtained as

$$\{(x, \mu, \lambda) |\ F(x, \mu, \lambda) = f(x, \mu) - \lambda = 0\} \tag{3.1}$$

To understand the complex structure of the equilibrium surface, $F(x, \mu, \lambda) = 0$, marked pink in Fig. 2a, we introduce two groups of planes $\mu =$ const and $\lambda =$ const to cut the equilibrium surface, respectively. The sections of $F(x, \mu, \lambda) = 0$ with $\mu < 1$, $\mu = 1$ and $\mu > 1$ can been seen in Fig. 2a, marked blue, which are also plotted in Fig. 2b in (λ, x) plane. While the sections of $F(x, \mu, \lambda) = 0$ with $\lambda < 0$, $\lambda = 0$ and $\lambda > 0$ are marked in Fig. 2a with white, black and green, respectively, which are also presented in Fig. 2c in (μ, x) plane.

Furthermore, to classify the nonlinear behaviour of the system, we define the generalized transition sets of double parameters (μ, λ) as following

$$\Sigma_g = \mathcal{B} \cup \mathcal{H} \cup \mathcal{S}, \tag{3.2}$$

where

$$\begin{aligned}
\mathcal{B} &= \Big\{(\mu, \lambda) |\ \exists x,\ \mu \in \mathbb{R},\ s.t.,\ F(x, \mu, \lambda) = F_x(x, \mu, \lambda) = 0,\ \mu \geqslant 0,\ \lambda \in \mathbb{R}\Big\} \\
\mathcal{H} &= \Big\{(\mu, \lambda) |\ \exists x,\ \lambda \in \mathbb{R},\ s.t.,\ F(x, \mu, \lambda) = F_x(x, \mu, \lambda) = F_{xx}(x, \mu, \lambda) = 0,\ \mu \geqslant 0,\ \lambda \in \mathbb{R}\Big\} \\
\mathcal{S} &= \Big\{(\mu, \lambda) |\ \exists x,\ \mu \in \mathbb{R},\ s.t.,\ F(x, \mu, \lambda) = 0,\ \forall \delta > 0,\ x_a = x - \delta,\ x_b = x + \delta, \\
&\qquad F_x(x_a) = F_x(x_b),\ \mu \geqslant 0,\ \lambda \in \mathbb{R}\Big\}
\end{aligned} \tag{3.3}$$

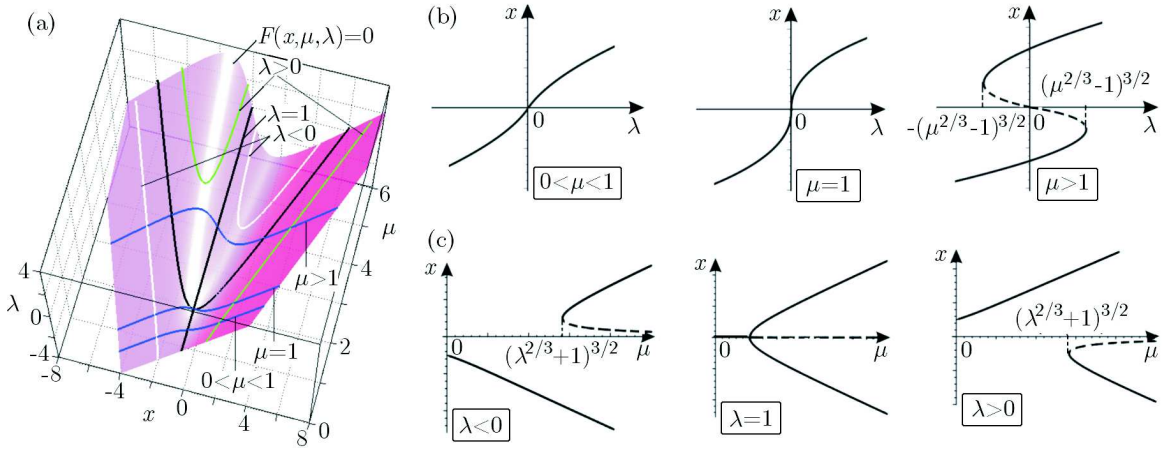

Fig. 2. (a) The equilibrium surface (pink) in space (x, μ, λ), (b) the sections cut by $\mu = 0.5, 1, 3$, (c) the sections cut by $\lambda = -1.5, 0, 1.5$ (colours online: http://www.ptmts.org.pl/volume.xsl?vol=52&no=1)

Here $\mathcal{B}$, $\mathcal{H}$ and $\mathcal{S}$ are the bifurcation set, hysteresis set and the symmetric set, respectively, which is obtained and written as

$$\begin{aligned} \mathcal{B} &= \{(\mu,\lambda)|\ \mu = (\lambda^{2/3}+1)^{3/2},\ \lambda \in \mathbb{R}\} \\ \mathcal{H} &= \{(\mu,\lambda)|\ \mu = 1,\ \lambda \in \mathbb{R}\} \\ \mathcal{S} &= \{(\mu,\lambda)|\ \mu \in \mathbb{R},\ \lambda = 0\} \end{aligned} \tag{3.4}$$

Meanwhile, the bifurcation set can be classified as

$$\mathcal{B} = \mathcal{B}_0 \cup \mathcal{B}_1 \cup \mathcal{B}_2 \tag{3.5}$$

where

$$\begin{aligned} \mathcal{B}_0 &= \{(\mu,\lambda)|\ \mu = 1, \lambda = 0\} \\ \mathcal{B}_1 &= \{(\mu,\lambda)|\ \mu = (\lambda^{2/3}+1)^{3/2},\ \lambda > 0\} \\ \mathcal{B}_2 &= \{(\mu,\lambda)|\ \mu = (\lambda^{2/3}+1)^{3/2},\ \lambda < 0\} \end{aligned} \tag{3.6}$$

Here $\mathcal{B}_1$ and $\mathcal{B}_2$ are a pair of saddle-centre (Diminnie and Haberman, 2000) bifurcation sets. Hence, the generalized transition can be described as

$$\Sigma_g = \mathcal{B}_0 \cup \mathcal{B}_1 \cup \mathcal{B}_2 \cup \mathcal{H} \cup \mathcal{S} \tag{3.7}$$

which bifurcates at the catastrophe point $A(\mu, \lambda) = (1, 0)$ and divides the parameter plane (μ, λ) into six persistent regions marked by IA, IIA, IIIA, IB, IIB, IIIB, as shown in Fig. $3\Sigma_g$. In each of these persistent regions, the system is structurally stable, while on Σ_g the system is structurally unstable. The corresponding phase portraits (black closed curves), restoring forces $F(x, \mu, \lambda) = f(x, \mu) - \lambda$ ($f(x, \mu)$ and λ marked blue and red, respectively) and the potentials $V(x)$ (marked green) are plotted in Figs. 3IA and $3\mathcal{B}_0$, respectively. The stability of the equilibrium of system (2.4) can be observed from the previous analysis Figs. 3IA and $3\mathcal{B}_0$, in which the stable equilibrium points (centers) correspond to the potential 'well' bottoms while the unstable ones (saddles or saddle-centres) correspond to the potential 'obstacle' summits.

It is worth noticing that the complex equilibrium bifurcations and the transitions are shown in Fig. 3 when the parameters vary over the parameter space, (μ, λ) plane, seen in Fig. $3\Sigma_g$. It is found that system (2.4) behaves as a pair of saddle-centre bifurcations from a single stable system into an asymmetrical bi-stable system via a saddle-centre bifurcation when the parameter point

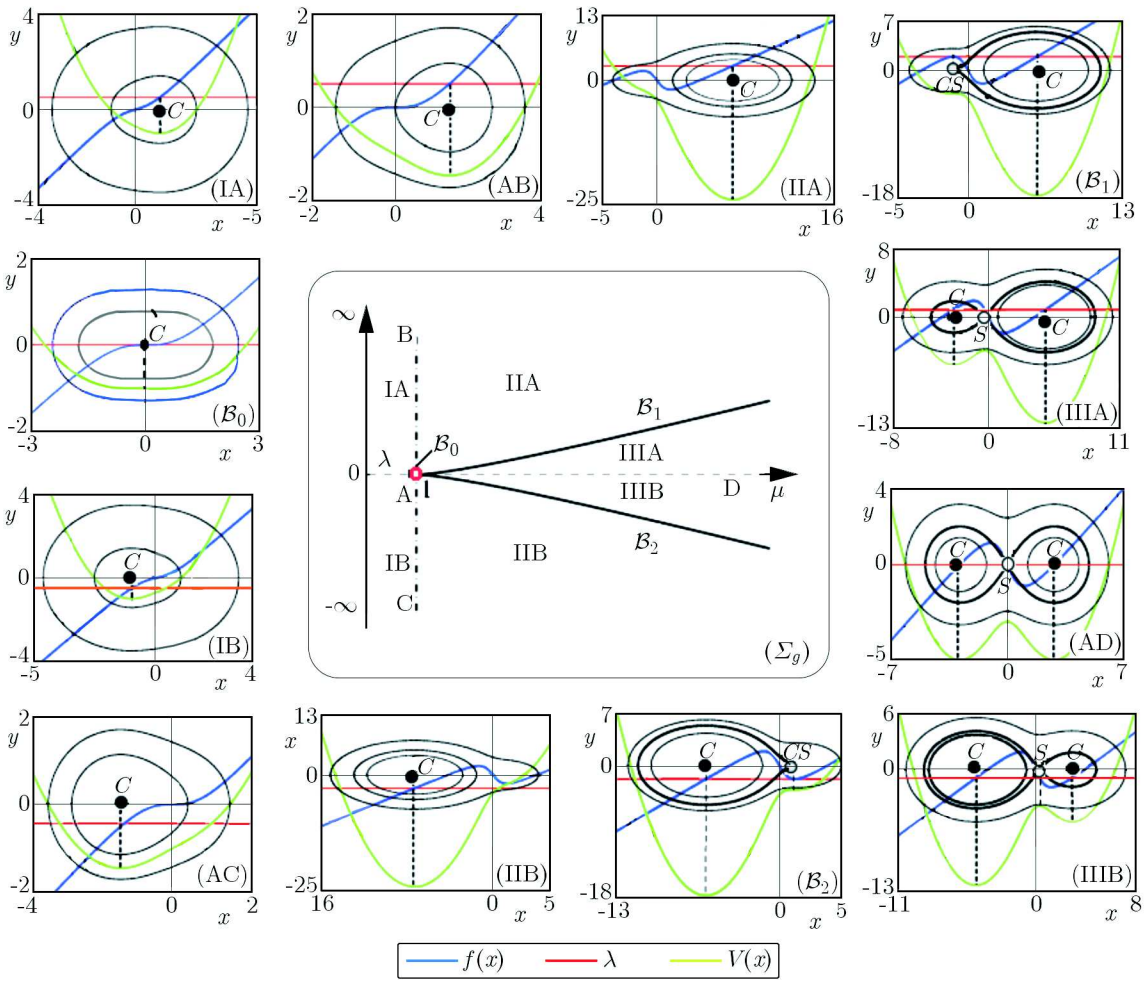

Fig. 3. Diagrams for the generalized transition set (Σ_g), and the related phase portraits, the centres marked with black bullets, the saddles marked with black hollow circles and the saddle-centres with grey bullets, with the corresponding restoring forces $f(x)$ (blue curves), λ (red lines) and the potentials $V(x)$ (green curves) (colours online: http://www.ptmts.org.pl/volume.xsl?vol=52&no=1)

(μ, λ) moves from region IIA into IIIA, or symmetrically from IIB into IIIB, crossing bifurcation the set $\mathcal{B}_1$, $\mathcal{B}_2$, respectively. A pitchfork bifurcation occurs when the parameter point (μ, λ) moves along the symmetric set $\mathcal{S}$ from $\mu < 1$ to $\mu > 1$ passing the catastrophe point A, seen in Figs. 3$\mathcal{B}_0$ and 3AD.

4. Parameter optimizations

In this Section, the SQZS and the maximum interval of the low frequency of the proposed model are obtained by parameter optimization, respectively.

4.1. Stable-quasi-zero-stiffness optimization

The stiffness of system (2.4) can be written as

$$K(x) = 1 - \frac{\mu}{\sqrt{(1+x^2)^3}} \tag{4.1}$$

which is plotted in Fig. 4a for different values of the parameter μ. The zero stiffness equilibrium points and the respective parameters can be obtained when $K(x) = 0$, $F(x) = 0$, that is,

$x = 0$, $\mu = 1$, $\lambda = 0$; $x = -\sqrt{\mu^{2/3} - 1}$, $\mu > 1$, $\lambda = \sqrt{(\mu^{2/3} - 1)^3}$; $x = \sqrt{\mu^{2/3} - 1}$, $\mu > 1$, $\lambda = -\sqrt{(\mu^{2/3} - 1)^3}$, as shown in Figs. $3\mathcal{B}_0$, $3\mathcal{B}_1$ and $3\mathcal{B}_2$, respectively. It can be seen from the stabilities shown in Figs. $3\mathcal{B}_0$, $3\mathcal{B}_1$ and $3\mathcal{B}_2$ that $x = 0$, $\mu = 1$, $\lambda = 0$ is the unique SQZS equilibrium.

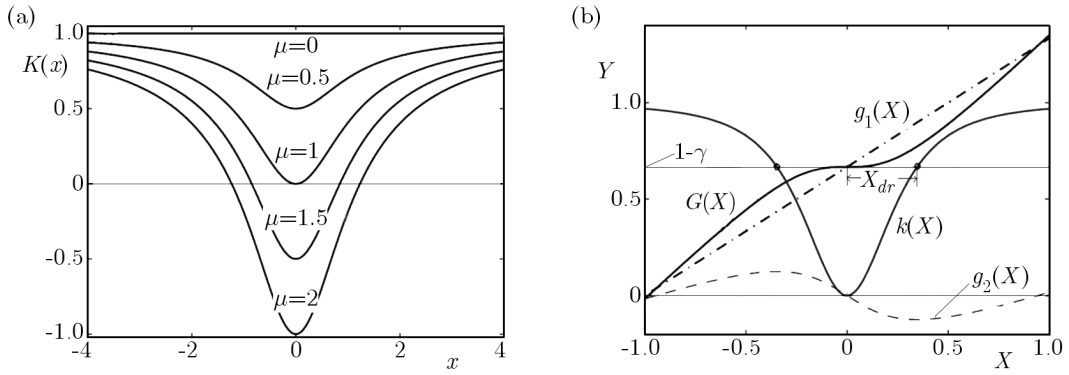

Fig. 4. Graphs for the dimensionless stiffness and restoring forces: (a) stiffness of system (2.4) for parameter $\mu = 0$, 0.5, 1.0, 1.5, 2.0, (b) total stiffness of system (2.2), marked $k(X)$, and the corresponding restoring force, marked $G(x)$, comprising the components of vertical and oblique springs, marked $g_1(X)$ with stiffness $1 - \gamma$ and $g_2(X)$, respectively, for $\alpha = \gamma = 0.5443$

4.2. Maximum interval of low frequency

Even the optimized parameters $\mu = 1$ and $\lambda = 0$ have been achieved for SQZS, it could not suggest the range of lower frequency. To obtain the maximum interval of lower frequency, further optimization is necessary for the parameter $\gamma(= \alpha)$. To do this, we will refocus our attention on system (2.2) with all the concern of the parameters $\mu = \gamma/\alpha$ in the following analysis, the dimensionless stiffness of which can be written as

$$k(X) = 1 - \frac{\alpha^2\gamma}{\sqrt{(\alpha^2 + X^2)^3}} \tag{4.2}$$

and the stiffness for the vertical spring denoted as $k_1 = 1 - \gamma$ correspondingly.

Consider the following control inequality

$$k(X) = 1 - \frac{\alpha^2\gamma}{\sqrt{(\alpha^2 + X^2)^3}} \leqslant \varepsilon k_1 \tag{4.3}$$

where $\varepsilon \in [0, 1]$ is the standard ratio. The excursion from $X = 0$ satisfying (4.3) can be obtained as

$$X_d = \gamma\sqrt{n^{-2/3} - 1} \tag{4.4}$$

where $n = 1 - \varepsilon(1 - \gamma)$, and the derivative of X_d with respective to γ can be obtained as

$$X_d'(\gamma) = \sqrt{n^{-2/3} - 1} - \frac{\varepsilon\gamma}{3n^{5/3}\sqrt{n^{-2/3} - 1}} \tag{4.5}$$

from which $\gamma \in [0, 1]$ can be optimized to maximize the lower frequency interval of X_d by letting $X_d'(\gamma) = 0$.

Figure 4b plots the restoring forces, $G(X)$ and $g_1(X)$, and the corresponding stiffness, $k(X)$ and k_1, in system (2.2) and the maximum dimensionless excursion X_d at the optimum value $\gamma = 0.5443$ when $\varepsilon = 1.0$. The details of the symbols can be seen in the above discussions and the corresponding captions.

5. Perturbed dynamics

In this Section, we investigate nonlinear dynamical phenomena for system (2.4) near the optimized parameter $\mu = 1$, $\lambda = 0$ when the system is subjected to a viscous damping and an external harmonic excitation with a amplitude f and frequency ω, written as the following

$$\ddot{x} + 2\zeta\dot{x} + x - \frac{\mu x}{\sqrt{1+x^2}} - \lambda = f\cos(\omega\tau). \tag{5.1}$$

5.1. Hamiltonian dynamics

Herein this subsection, the resonance behaviour of system (5.1) without damping ($\zeta = 0$) is investigated by the Hamiltonian

$$H_f(x, y, \tau) = \frac{1}{2}x^2 + \frac{1}{2}y^2 - \mu\sqrt{1+x^2} - fx\cos(\omega\tau) \tag{5.2}$$

which is one and a half degree of freedom system and time τ is regarded as a parameter.

To construct an extended phase space (x, y, E, τ), $E = -H_f$ is treated as another additional coordinate, acting as the conjugate momentum of τ, while the flow in the extended space is described by an auxiliary parameter ξ playing the role of time (Lichtenberg and Lieberman, 1992; Cao *et al.*, 2011).

The new Hamiltonian H_E can be obtained via the generating function $F_{2(1)}(x, y, E, \tau) = xy + E\tau$ and written as in following form

$$H_E(x, y, E, \tau) = \frac{1}{2}x^2 + \frac{1}{2}y^2 + E - \mu\sqrt{1+x^2} - fx\cos(\omega\tau) = \mathcal{E} \tag{5.3}$$

which is dynamically similar to a two-degree-of-freedom autonomous system and still non-integrable owing to the lack of other first integral besides (5.3) $\mathcal{E} = \text{const}$ (Freitas and Viana, 2004).

The first two terms in the above extended Hamiltonian denote a harmonic oscillator for which a pair of action and angle variables J, θ with the definition $x = \sqrt{2J}\sin\theta$ and $y = \sqrt{2J}\cos\theta$ can be introduced, and Hamiltonian (5.3) is written as

$$H_a(J, E; \theta, \tau) = J + E - \mu\sqrt{1 + 2J\sin^2\theta} - f\sqrt{2J}\sin\theta\cos(\omega\tau) \tag{5.4}$$

To obtain the dynamical torus, we introduce another canonical transformation by means of the generating function $F_{2(2)}(J_\theta, J_\varphi; \theta, \varphi) = \omega_\varphi\tau J_\varphi + \theta J_\theta$, such that the phase space (J, θ, E, τ) is transformed into J_θ, J_φ, θ, φ defined by $J_\theta = J$, $\theta = \theta$, $J_\varphi = E/\omega$ and $\varphi = \omega\tau$ (Cao *et al.*, 2011).

The new Hamiltonian in action-angular space $(J_\theta, J_\varphi, \theta, \varphi)$ can be written as

$$\begin{aligned} H(J_\theta, J_\varphi; \theta, \varphi) &= H_0(J_\theta, J_\varphi) + H_1(J_\theta, J_\varphi; \theta, \varphi) \\ &= \omega_\theta J_\theta + \omega_\varphi J_\varphi - \mu\sqrt{1 + 2J_\theta\sin^2\theta} - f_0\sqrt{2J}\sin\theta\cos\varphi \end{aligned} \tag{5.5}$$

which describes motions of the system on the extended torus.

For convenience, it is assumed that $\varphi = \omega_\varphi\tau \mod 2\pi$ and $\varphi = 0$ is equivalent to $T = 2\pi/\omega$. In the unperturbed Hamiltonian of system (5.5), there exist two frequencies

$$\omega_\varphi = \frac{\partial H_{a0}}{\partial J_\varphi} = \omega \qquad \omega_\theta = \frac{\partial H_{a0}}{\partial J_\theta} \tag{5.6}$$

where ω_φ, ω_θ are the external frequency and the natural frequency of the system, respectively. The behaviour of the forced system is restricted in a torus with both action and angular variables

ω_φ and ω_θ, which can be described by the definition of the winding number $\alpha = \omega_\theta/\omega_\varphi$. Here ω_θ and ω_φ are the rotating frequencies along the cycles of latitude and cycles of longitude along the torus while J_θ and J_φ retain two constants corresponding to ω_θ and ω_φ for a given initial value in (5.5), respectively. The most interesting case of the behaviour is the resonance which happens when $m\omega_\theta - n\omega_\varphi = 0$, where m and n are a pair of related prime integers. The behaviour is harmonic resonance if $m = n = 1$, sub-harmonic resonance of m order if $m > 1$, $n = 1$, super-harmonic resonance of n order if $m = 1$, $n > 1$, and super-sub-harmonic resonance if $m > 1$, $n > 1$ (Lichtenberg and Lieberman, 1992). The winding number $\alpha = m/n$ can be observed in that m and n are corresponding to the number of fixed points and the number of twists of the trajectories dividing by their greatest common factor in the Poincaré section, respectively. In addition, if the winding number α is irrational, the trajectory never closes on itself filling a torus densely, for which the map in the Poincaré section exhibits a generic KAM curve, namely a quasi-periodic motion. The following numerical simulations are presented in the form of Poincaré sections taken at zero phase angle by a stroboscopic time-T map of $T = 2\pi/\omega$ for different initial values and trajectories on the phase plane for the optimized system depicted by Eq. (5.2).

Figure 5a demonstrates the Poincaré section calculated for $\zeta = 0$, $\mu = 1$, $\lambda = 0$, $f = 0.5$ and $\omega = 1.086$, which presents the complex KAM structure (Cao *et al.*, 2008b; Lichtenberg and Lieberman, 1992). A peculiar orbit identified as a chaotic sea or stochastic web can be found, which fills the finite area and connects the isolated islands encircling the associated series of fixed points (one prime resonant period 1 solution, marked purple, with the secondary resonances of period 3, marked grey; a pair of period 2, marked black and dark red, with the corresponding secondary resonances of period 6, marked light blue and green, respectively; one period 5, marked cyan and a pair of period 3, marked light green and orange, with the corresponding secondary resonances of period 6, marked light blue and dark green, respectively). As can be seen from this figure, there exist KAM curves and a series of fixed points outside of the finite region (period 13 closed to the chaotic sea, a pair of period 4 of the outmost resonances, marked green and red, respectively, and a series period 7 fixed points) with the associated quasi-periodic islands connected by chaotic orbits. As for examples, Fig. 5b-5g plot some of the resonant trajectories and the corresponding Poincaré section given in Fig. 5a: Figs. 5b,c,d and 5e for prime resonances of period 1, period 2, period 5 and period 3 solutions, respectively, and, Figs. 5f and 5g for the secondary resonances of period three and period six associated period one and period two resonances, respectively.

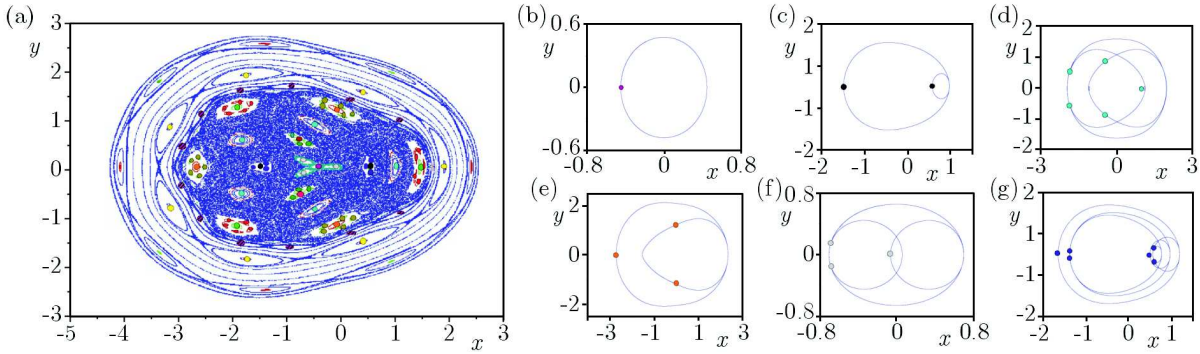

Fig. 5. (a) Global KAM structure ($\zeta = 0$, $\mu = 1$, $\lambda = 0$, $f = 0.50$, $\omega = 1.086$); (b)-(e) the resonant fixed points and the corresponding trajectories of period 1, 2, 5 and period 3, respectively, (f) and (g) the secondary resonances of period 3 and period 6 associated with the period 1 and period 2 plotted in (b) and (c), respectively (colours online: http://www.ptmts.org.pl/volume.xsl?vol=52&no=1)

Figure 6 demonstrates the existence of invariant curves with hyperbolic fixed points surrounding the elliptic fixed points (Guckenheimer and Holmes, 1999), which results in the sudden

change to chaotic sea when the parameter varies. Figure 6a presents the complex KAM structure with KAM curves, hyperbolic fixed points connecting invariant curves of homoclinic and heteroclinic types surrounding the elliptic fixed points for $\mu = 1$, $\zeta = 0$, $\lambda = 0$, $f = 0.40$, $\omega = 0.50$. While Fig. 6b plots the KAM structure, for $\mu = 1$, $\zeta = 0$, $\lambda = 0$, $f = 0.45$, $\omega = 0.50$, with a chaotic sea burst from the broken of the invariant curves and one period one and two pairs of period two resonances preserved from the former KAM structure, which implies a very complicated bifurcation procedure for further investigation.

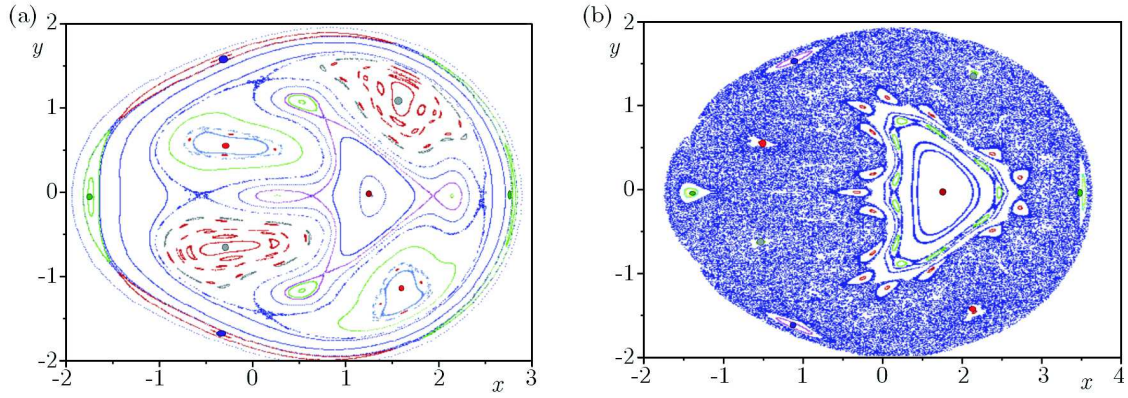

Fig. 6. Global KAM structure on Poincaré sections: (a) for $\zeta = 0$, $\mu = 1$, $\lambda = 0$, $f_0 = 0.40$, $\omega = 0.50$, (b) for $\zeta = 0$, $\mu = 1$, $\lambda = 0$, $f_0 = 0.45$, $\omega = 0.50$
(colours online: http://www.ptmts.org.pl/volume.xsl?vol=52&no=1)

5.2. Driven system with dissipation

In this subsection, we will focus our attention on the detailed complex behaviour of period doubling, multiple stability (Freitas and Viana, 2004), chaos crisis (Hong and Hu, 1999, 2004), saddle-node bifurcation (Nusse *et al.*, 1995) and the transient chaos (Grebogi *et al.*, 1983; Souza *et al.*, 2004, 2008), etc., by examining the bifurcation diagram of system (5.1). The diagram is plotted in Fig. 7a for the stroboscopically sampled displacement x versus the control parameter μ near the optimized parameters $\mu = 1$, $\lambda = 0$ with $\zeta = 0.027$, $f = 0.40$ and $\omega = 0.26$, for which the corresponding Lyapunov exponent (Wolf *et al.*, 1985) diagram is given in Fig. 7b, while the corresponding rectangled areas are enlarged in Figs. 7c and 7d, respectively.

5.2.1. Coexisted period doubling bifurcation

It can be seen from Fig. 7a or clearly in Fig. 7c, that a pair of coexisted period doublings (marked red and blue) bifurcated from a period 1 solution via symmetry-breaking bifurcation at $\mu = 0.9302$ lead to the corresponding coexisted chaotic attractors, respectively. The corresponding phase portraits for the period doubling marked in blue shown in Fig. 7c are plotted in Figs. 8a-8d for the period 1, period 2, period 4, and a small chaotic attractors for $\mu = 0.960$, 0.977, 0.980 and 0.984, respectively, while the corresponding coexisted chaotic attractor for $\mu = 0.984$ is shown in Fig. 8e led by the period doubling marked red.

As the parameter μ increases to 0.9884, the interior crises burst out, which arises from the collisions between the coexisted chaotic attractors and the saddles within the corresponding basins of attraction. The corresponding phase portrait with the Poincaré section is plotted in Fig. 8f. In addition, Fig. 7c also shows the boundary crisis of chaos as μ increases again to $\mu = 1.0042$, which is originated from the collision between the chaotic attractor and the unstable periodic attractor on the boundary of its basin.

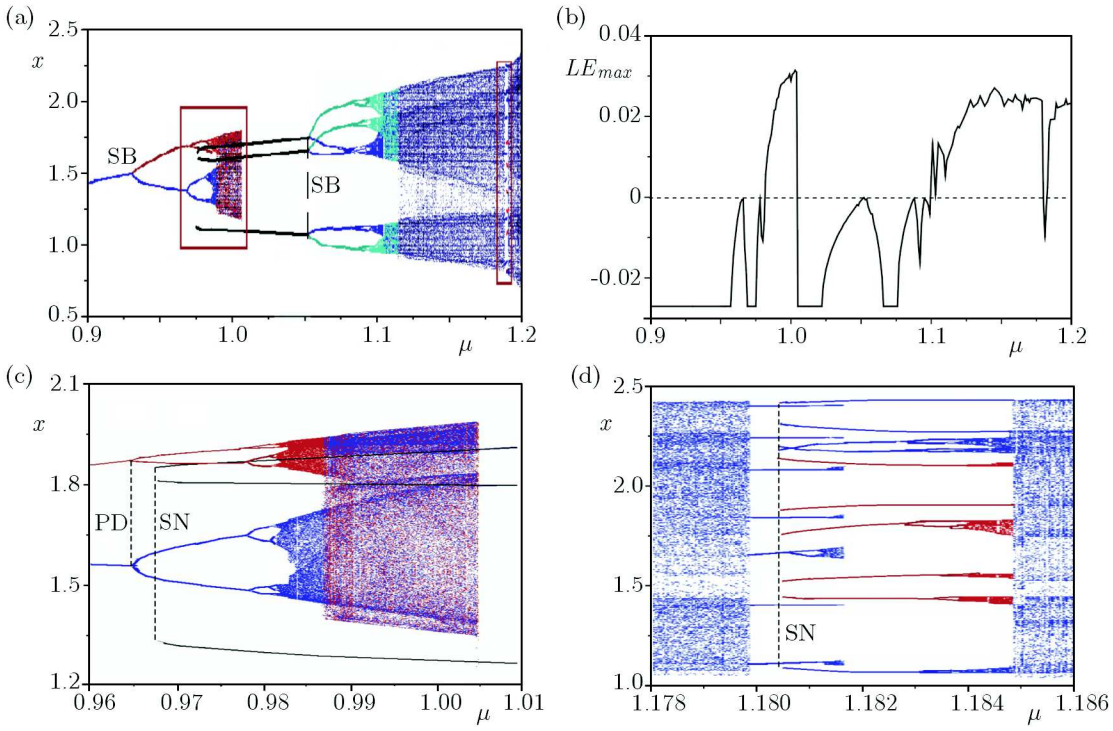

Fig. 7. (a) Bifurcation diagram of x versus μ with symmetry-breakings marked with SB for $\zeta = 0.027$, $\lambda = 0$, $f = 0.40$, $\omega = 0.26$, (b) the corresponding maximum Lyapunov exponent for (a) with initial condition $(2, 0)$, (c) and (d) the enlarged diagram of the left and right rectangle area in Fig. 7a, respectively, with period doubling (PD) and saddle-node bifurcations (SN) (colours online: http://www.ptmts.org.pl/volume.xsl?vol=52&no=1)

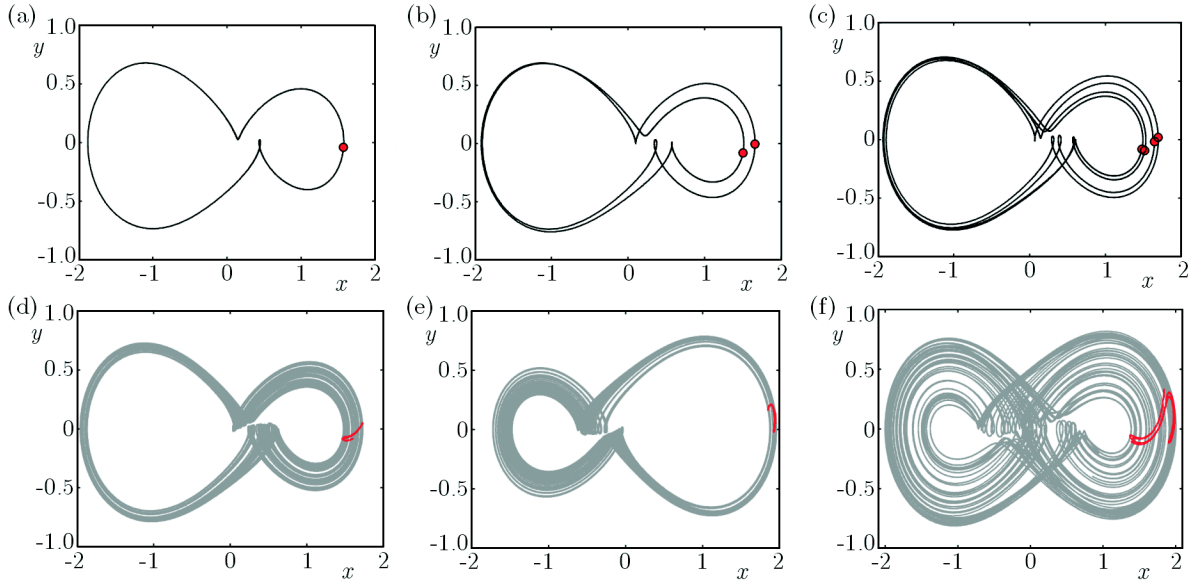

Fig. 8. Phase portraits and Poincaré sections of period 1 doubling for $\zeta = 0.027$, $\lambda = 0$, $f = 0.40$, $\omega = 0.26$, (a) $\mu = 0.960$, (b) $\mu = 0.977$, (c) $\mu = 0.980$, (d) $\mu = 0.984$, showing the period 1, 2, 4, and chaotic motion corresponding to the blue bifurcation diagram in Fig. 7c, (e) $\mu = 0.984$, (f) $\mu = 1.000$ (colours online: http://www.ptmts.org.pl/volume.xsl?vol=52&no=1)

5.2.2. Multiple stability and saddle-node bifurcation

It can also be seen from Fig. 7a that a period 3 solution (marked black) occurs at $\mu = 0.9689$, which is coexisted with the above pair of period doublings, bifurcates into a pair of period 3

solutions at $\mu = 1.0521$ leading to chaos (marked blue and cyan) via period doubling, and then the interior crises to a larger chaotic attractor at $\mu = 1.1122$.

Basin analysis (Hsu, 1992; Nusse and Yorke, 1994) demonstrates the complex co-existence of multiple stable solutions using Poincaré sections (coloured bullets), as shown in Fig. 9, and the coexistence of a pair of period 3 solutions, one stable and the other unstable, which denotes the burst of a saddle-node bifurcation at $\mu = 0.9689$, as shown in Fig. 7c. The basins (marked cyan and pink) of a pair of period 1 solutions (red and yellow) are shown for $\mu = 0.96$ in Fig. 9a; Fig. 9b plots the basins (marked cyan, pink and white, respectively) of a pair period 2 (red and yellow) and a period 3 (green) solutions when $\mu = 0.977$, on the boundaries of which there exists an unstable period 3 solution (the hollow black squares) accompanied with the stable one; in the same way, as shown in Fig. 9c for $\mu = 0.984$, there also occurs the unstable period 3 solution (the hollow black squares) on the boundaries of basins (cyan, pink and white, respectively) of the pair of chaotic attractors (red and yellow) led by period doubling from the periodic solutions and the stable periodic solution (green) above. While Fig. 9d presents the basins (white) of the chaotic attractor (marked blue), merged from the pair of the small chaotic attractor above, and the stable period 3 solution (green bullets), where the unstable period 3 attractor (hollow black squares) still retains on the basin boundary.

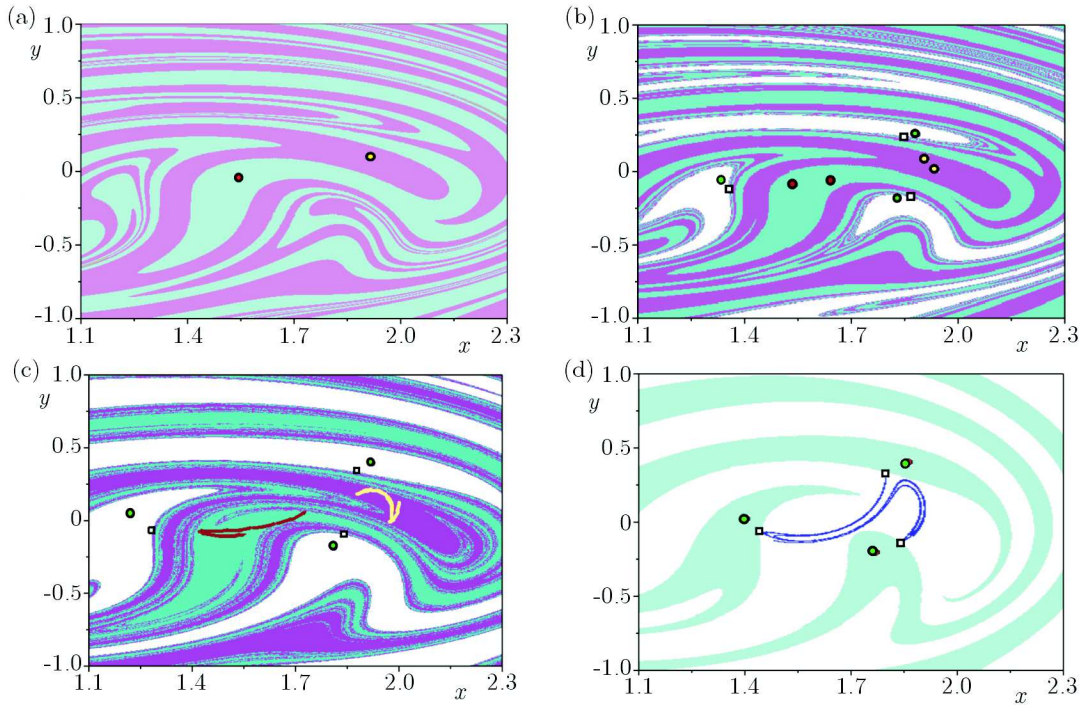

Fig. 9. Attraction basins and their corresponding co-existed attractors for $\zeta = 0.027$, $\lambda = 0$, $f = 0.40$, $\omega = 0.26$: (a) $\mu = 0.960$, (b) $\mu = 0.977$, (c) $\mu = 0.984$, (d) $\mu = 1$
(colours online: http://www.ptmts.org.pl/volume.xsl?vol=52&no=1)

5.2.3. Periodic motions and their transients

Numerical investigations are also carried out for evidencing bifurcation phenomena displayed in Fig. 7d, which is the enlargement of the right rectangled area in Fig. 7a. At the critical value $\mu = 1.1798$, there occurs a crisis such that the chaotic attractor disappears suddenly jumping to a period 7 orbit (the phase portrait for $\mu = 1.1802$ shown in Fig. 10a). The period 7 solution stops short at $\mu = 1.1817$ via a doubling-period bifurcation cascade ($\mu = 1.1814$) (Thompson and Stewart, 2002) remaining a pair of coexisted stable period 5 solutions occurring via saddle-

-node bifurcation (SN) at $\mu = 1.1804$ (Fig. 10b plots the period 5 trajectories with the Poincaré sections for $\mu = 1.1812$), which leads to a merged chaotic attractor at $\mu = 1.1851$, as shown in Fig. 10d.

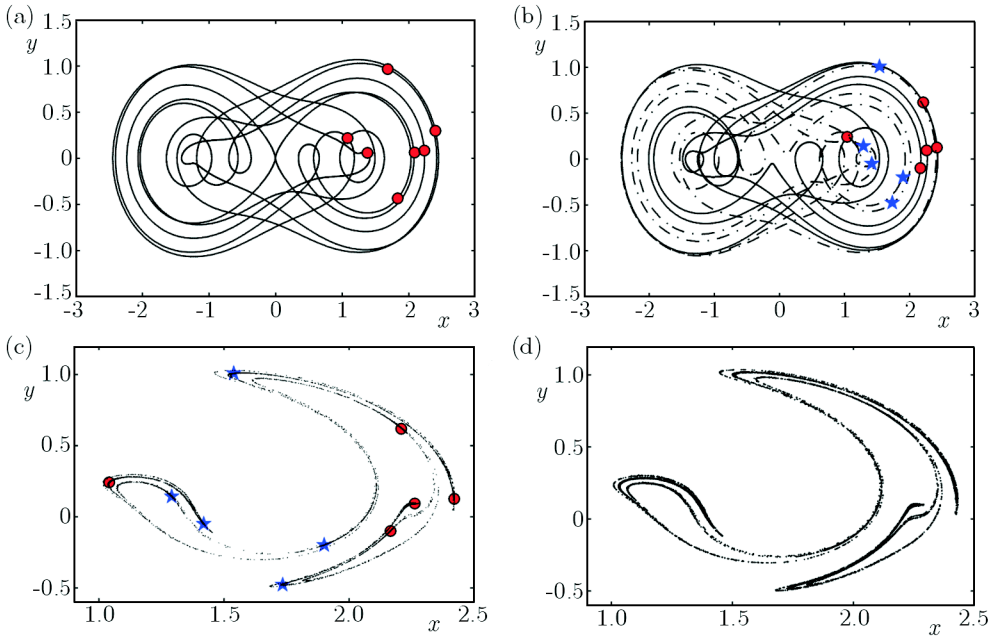

Fig. 10. Trajectories and Poincaré sections for $\zeta = 0.027$, $\lambda = 0$, $f = 0.40$, $\omega = 0.26$: (a) $\mu = 1.1802$, (b) and (c) $\mu = 1.1812$, transient chaos and period five solutions, and (d) $\mu = 1.1851$, chaotic attractor (colours online: http://www.ptmts.org.pl/volume.xsl?vol=52&no=1)

A transient chaos is also found at $\mu = 1.1812$ to be a non-attracting chaotic saddle, which settles down to one of the period 5 motions depending on the initial conditions, as shown in Fig. 10c. The life of the transient chaos can be demonstrated via the time-series, as shown in Fig. 11a-c for the initial values $(-1.0, 0)$, $(2.1, 0)$ and $(1.0, 0)$, respectively, with different durations of the chaotic saddles.

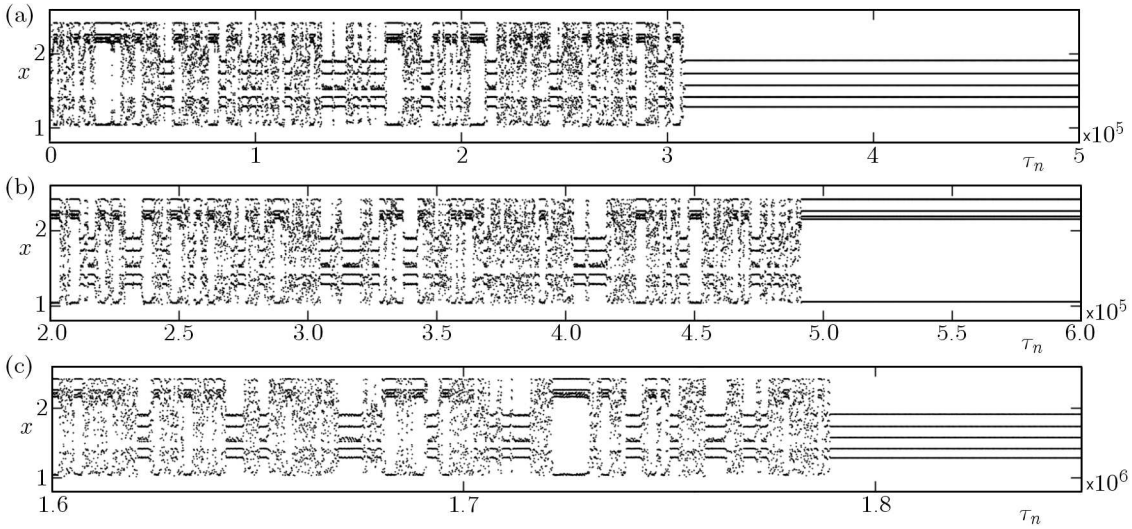

Fig. 11. Time-series of stroboscopic map for discrete displacements x versus time τ_n ($\tau_n = 2n\pi/\omega$, $n = 0, 1, 2, \ldots$) for $\mu = 1.1812$

6. Conclusions

In this paper, a novel dynamical model with SQZS has been proposed for GVT of large scale aircraft or isolations systems. The equilibrium bifurcations and the stabilities of the unperturbed system are presented to get the SQZS optimization for parameters at $\mu = 1$, $\lambda = 0$ and the maximum low stiffness interval has been achieved for α and γ. Further studies near the optimized parameters showed complex KAM structures with complicated resonances for the forcing system and the complex dynamics of the system perturbed by both viscous damping and external forcing. The results presented herein this paper enable us to get a better understanding of the mechanism of the dynamical design for the low frequency supporting or isolation systems. The investigations for the presented model are carried out by the current authors in two main directions. The first possible direction is to explore further nonlinear dynamics of asymmetry of Hopf bifurcations and the co-dimension behaviour for the optimized system, and the second direction is the experimental investigation for further dynamical parameter design.

Acknowledgement

This work is supported by the National Natural Science Foundation of China (Grant No. 11072065 and 10932006). We also acknowledge the valuable discussions and suggestions with Prof. Jingtang Xing, Faculty of Engineering and the Environment, the University of Southampton, Southampton SO17 1BJ, UK.

References

1. Alabuzhev P., Gritchin A., Kim L., 1989, *Vibration Protecting and Measuring Systems with Quasi-Zero Stiffness*, Hemisphere Publishing Co., Taylor & Francis Group, New York
2. Arafat R.M.D., Park S.T., Sajal C.B., 2010, Design of a vehicle suspension system with negative stiffness system. *IST Transaction of Mechanical System Theoretic and Application*, **1**, 2, 1-7
3. Blair D.G., Winterflood J., Slagmolen B., 2002, High performance vibration isolation using springs in Euler column buckling mode, *Physics Letters A*, **300**, 122-130
4. Breban R, Nusse H.E., Ott E., 2003, Lack of predictability in dynamical systems with drift: scaling of indeterminate saddle-node bifurcations, *Physical Letter A*, **319**, 79-84
5. Cao Q.J., Xiong Y.P., Wiercigroch M., 2011, Resonances of the SD oscillator due to the discontinuous phase, *Journal of Applied Analysis and Computation*, **1**, 2, 183-191
6. Cao Q.J., Wang D., Chen Y.S., Wiercigroch M., 2012, Irrational elliptic functions and the analytical solutions of SD oscillator, *Journal of Theoretical and Applied Mechanics*, **50**, 3, 701-715
7. Cao Q.J., Wiercigroch M., Pavlovskaia E.E., 2006, An archetypal oscillator for smooth and discontinuous dynamics, *Physical Review E*, **74**, 046218
8. Cao Q.J., Wiercigroch M., Pavlovskaia E.E., 2008a, Piecewise linear approach to an archetypal oscillator for smooth and discontinuous dynamics, *Philosophical Transactions R. Soc. London. Series A. Mathematical, Physical and Engineering*, **366**, 635-653
9. Cao Q.J., Wiercigroch M., Pavlovskaia E.E., 2008b, The limit case response of the archetypal oscillator for smooth and discontinuous dynamics, *International Journal of Non-Linear Mechanics*, **43**, 462-473
10. Carrella A., Brennan M.J., Waters T.P., 2007, Static analysis of a passive vibration isolator with quasi-zero-stiffness characteristic, *Journal of Sound and Vibration*, **301**, 3/5, 678-689
11. Denoyer K., Johnson C., 2001, Recent achievements in vibration isolation systems for space launch and

12. Diminnie D.C., Haberman R., 2000, Slow passage through a saddle-center bifurcation, *Journal of Nonlinear Science*, **10**, 197-221

13. Freitas M.S.T., Viana R.L., 2004, Multistability, basin boundary structure, and chaotic behaviour in a suspension bridge model, *International Journal of Bifurcation and Chaos*, **14**, 3, 927-950

14. Grebogi C., Ott E., Yorke J.A., 1983, Crises, sudden changes in chaotic attractors, and transient chaos, *Physica D*, **173**, 181-200

15. Green G.S., 1945, The effect of flexible ground supports on the pitching vibrations of an aircraft, *R&M 2291*, November

16. Guckenheimer J., Holmes P., 1999, *Nonlinear Oscillation. Dynamical System and Bifurcation of Vector Fields*, Springer-Verlag, New York

17. Hong L., Xu J.X., 1999, A chaotic crisis and chaotic transients studied by the generalized cell mapping digraph method, *Physical Letter A*, **262**, 361-375

18. Hong L., Xu J.X., 2004, Crisis and chaotic saddle and attractor in forced Duffing oscillator, *Communication of Nonlinear Science Numerical Simulation*, **9**, 313-329

19. Hsu C.S., 1992, Global analysis by cell mapping, *International Journal of Bifurcation and Chaos*, **2**, 4, 727-771

20. Ibrahim R.A., 2008, Recent advances in nonlinear passive vibration isolators, *Journal of Sound and Vibration*, **314**, 371-452

21. Kovacic I., Brennan M.J., Waters T.P., 2008, A study of a non-linear vibration isolator with a quasi-zero stiffness characteristic, *Journal of Sound and Vibration*, **315**, 700-711

22. Lai S.K., Xiang Y., 2010, Application of a generalized Senator-Bapat perturbation technique to nonlinear dynamical systems with an irrational restoring force, *Computers and Mathematics with Applications*, **60**, 7, 2078-2086

23. Lichtenberg A.J., Lieberman M.A., 1992, *Regular and Chaotic Dynamics* Springer-Verlag, New York

24. Lorrain P., 1974, Low natural frequency vibration isolator or seismograph,*Review of Science Instrument*, **45**, 198-202

25. Molyneux W.G., 1957, Supports for vibration isolation, *A.R.C., Current Paper*, **322**

26. Nusse H.E., Ott E., Yorke J.A., 1995, Saddle-node bifurcations on fractal basin boundaries, *Physical Review Letter*, **75**, 2482-2485

27. Nusse H.E., Yorke J.A., 1994, *Dynamics: Numerical Explorations*, Applied Mathematical Sciences, Vol 101, Springer-Verlag, New York

28. Platus D.L., 1992, Negative-stiffness-mechanism vibration isolation systems, *Proceedings of SPIE. Vibration Control in Microelectronics, Optics, and Metrology*, San Jose, CA, USA, **1619**, 44-54

29. Souza S.L.T., Caldas I.L., Viana R.L., 2004, Sudden changes in chaotic attractors and transient basins in a model for rattling in gearboxes, *Chaos, Solition and Fractals*, **21**, 763-772

30. Souza S.L.T., Caldas I.L., Viana R.L., Balthazar J.M., 2008, Control and chaos for vibro-impact and non-ideal, *Jounal of Theoretical and Applied Mechanics*, **46**, 3, 641-664

31. Thompson J.M.T., Stewart H.B., 2002, *Nonlinear Dynamics and Chaos*, 2nd ed., Wiley, London

32. Tian R.L., Cao Q.J., Yang S.P., 2010, The codimention-two bifurcation for the recent proposed SD oscillator, *Nonlinear Dynamics*, **59**, 19-27

33. Winterflood J., 2001, High performance vibration isolation for gravitational wave detection, Ph.D. Thesis, University of Western Australia, Western Australia

34. Wolf A., Swift J.B., Swinney H.L., 1985, Determining Lyapunov exponents from a time series, *Physica D*, **16**, 285

35. Xing J.T., Xiong Y.P., Price W.G., 2005, Passive-active vibration isolation systems to produce zero or infinite dynamic modulus: theoretical and conceptual design strategies, *Journal of Sound and Vibration*, **286**, 615-636

36. Zhang J.Z., Li D., Chen M.J., 2004, An ultra-low frequency parallel nonlinear isolator for precision instruments, *Key Engineering Material*, **57**, 258, 231-236 on-orbit applications, *52nd International Astronautics Congress*, Toulouse, France

Manuscript received May 21, 2013; accepted for print September 2, 2013